

Structure Inversion Asymmetry and Rashba Effect in Quantum Confined Topological Crystalline Insulator Heterostructures

Rafał Rechciński,* Marta Galicka, Mathias Simma, Valentine V. Volobuev, Ondřej Caha, Jaime Sánchez-Barriga, Partha S. Mandal, Evangelos Golias, Andrei Varykhalov, Oliver Rader, Günther Bauer, Perla Kacman, Ryszard Buczko, and Gunther Springholz*

Structure inversion asymmetry is an inherent feature of quantum confined heterostructures with non-equivalent interfaces. It leads to a spin splitting of the electron states and strongly affects the electronic band structure. The effect is particularly large in topological insulators because the topological surface states are extremely sensitive to the interfaces. Here, the first experimental observation and theoretical explication of this effect are reported for topological crystalline insulator quantum wells made of $\text{Pb}_{1-x}\text{Sn}_x\text{Se}$ confined by $\text{Pb}_{1-y}\text{Eu}_y\text{Se}$ barriers on one side and by vacuum on the other. This provides a well defined structure asymmetry controlled by the surface condition. The electronic structure is mapped out by angle-resolved photoemission spectroscopy and tight binding calculations, evidencing that the spin splitting decisively depends on hybridization and, thus, quantum well width. Most importantly, the topological boundary states are not only split in energy but also separated in space—unlike conventional Rashba bands that are splitted only in momentum. The splitting can be strongly enhanced to very large values by control of the surface termination due to the charge imbalance at the polar quantum well surface. The findings thus, open up a wide parameter space for tuning of such systems for device applications.

applications.^[1–4] Due to their non-trivial topology of electronic band structure, gapless 2D states of zero-mass electrons emerge at the surface whose wave functions decay exponentially into the bulk. In these states, the electron spin is locked to the momentum and the energy spectrum is described by Dirac cones connecting the valence with the conduction band.^[1–3] In TI heterostructures a variety of novel features such as the quantum anomalous Hall effect^[5,6,12,13] and quantum spin Hall effect (QSHE)^[7–11] occur, which open up promising pathways for quantum electronic device applications.^[6,14–16]

For practical TI devices, thin film geometries are needed to minimize the bulk transport contribution. If the film thickness is very small, the wave functions of the topological surface states (TSS) at opposing film boundaries overlap and hybridize. This opens an energy gap near the time reversal symmetric (TRS) point and the electrons gain mass, as theoretically predicted^[17–22] and experimentally observed.^[23–25] In addition, when the film thickness is below the de Broglie wavelength of the electrons, quantized 2D subbands are formed due to the confinement of the electrons by the surrounding potential barriers. This occurs both for topologically trivial as well


1. Introduction

Topological insulators (TIs) and topological crystalline insulators (TCIs) have attracted tremendous interest due to their outstanding electronic properties and vast potentials for device

applications.^[17–22] and experimentally observed.^[23–25] In addition, when the film thickness is below the de Broglie wavelength of the electrons, quantized 2D subbands are formed due to the confinement of the electrons by the surrounding potential barriers. This occurs both for topologically trivial as well

R. Rechciński, Dr. M. Galicka, Prof. P. Kacman, Prof. R. Buczko
Institute of Physics
Polish Academy of Sciences
Aleja Lotników 32/46, Warsaw PL-02-668, Poland
E-mail: rafal.rechcinski@ifpan.edu.pl

M. Simma, Dr. V. V. Volobuev, Prof. G. Bauer, Prof. G. Springholz
Institute for Semiconductor and Solid State Physics
Johannes Kepler University
Altenberger Str. 69, Linz 4040, Austria
E-mail: gunther.springholz@jku.at

 The ORCID identification number(s) for the author(s) of this article can be found under <https://doi.org/10.1002/adfm.202008885>.

© 2021 The Authors. Advanced Functional Materials published by Wiley-VCH GmbH. This is an open access article under the terms of the Creative Commons Attribution License, which permits use, distribution and reproduction in any medium, provided the original work is properly cited.

DOI: 10.1002/adfm.202008885

Dr. V. V. Volobuev
International Research Centre MagTop, Institute of Physics, Polish Academy of Sciences, Aleja Lotników 32/46, PL-02668 Warsaw Poland and National Technical University “KhPI”
Kyrpychova Str. 2, Kharkiv 61002, Ukraine

Dr. O. Caha
Department of Condensed Matter Physics
Masaryk University
Kotlářská 2, Brno 61137, Czech Republic

Dr. J. Sánchez-Barriga, Dr. P. S. Mandal, Dr. E. Golias, Dr. A. Varykhalov, Prof. O. Rader
Helmholtz-Zentrum Berlin für Materialien und Energie
Elektronenspeicherring BESSY II, Berlin 12489, Germany

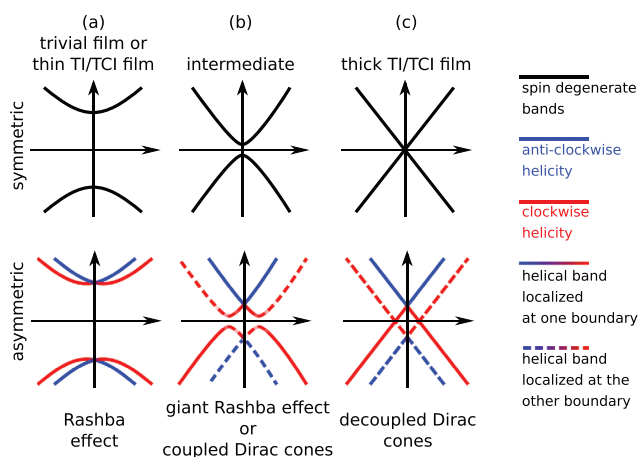


Figure 1. Schematic energy versus momentum diagrams of the low-energy electronic structure of topological (crystalline) insulator (TI/TCI) films with inversion symmetric (upper row) and with inversion asymmetric structure (lower row). (a) For ultra thin TI/TCI films a band gap opens due to the hybridization of the topological surface and interface states that are in close proximity to each other. With SIA superimposed (lower panel), the bands split up into two spin polarized Rashba branches of opposite helicity, as indicated by the blue and red color, respectively, similar as in a trivial normal insulator film. (b) For intermediate thick films the interface coupling is reduced but the hybridization still effective. This leaves the gap open and but coupled massive Dirac cones appear. (c) Further increasing TI/TCI film thickness leads to a decoupling of the topological surface/interface states. For symmetric structures (upper panel) a single, doubly degenerate and gapless Dirac cone is formed due to the superposition of oppositely spin-polarized TSSs from both interfaces for which reason, the net spin polarization over the entire film is zero. Conversely, for asymmetric structures (lower panel of (c)) the two Dirac cones are decoupled and shifted vertically with respect to each other. The dashed/solid lines indicate that each one of these Dirac cones is localized at one of the two film boundaries.

as non-trivial systems. The size quantization monotonically decreases with increasing layer thickness, but the hybridization gap can oscillate and may even change sign, which in turn changes the topological character of the system.^[10,11,19–22]

For ideal inversion symmetric films with perfectly identical surfaces/interfaces, the hybridization gap opens exactly at the

TRS point and the hybridized TSSs are doubly degenerate as illustrated by the upper panels of **Figure 1**. In real world structures, however, grown on a substrate, the top surface and bottom interface are always different. As a result, the Dirac points (DP) split up due to the broken structure inversion symmetry and the hybridization gap appears away from the TRS point^[20,25,26] (see lower panels of **Figure 1**). This is reminiscent of the giant Rashba effect in normal trivial insulators (NI).^[27–30] Once, however, the film thickness exceeds the TSS localization length, the surface states at the film boundaries become independent of each other and the hybridization gap vanishes. This leaves two independent spin polarized Dirac cones, each located at one of the opposite interfaces. In each of the three cases shown in **Figure 1**, the structure inversion asymmetry (SIA) induces a spin splitting of the electronic bands. We understand that any such spin splitting falls under the definition of the Rashba effect, i.e., momentum dependent conventional Rashba effect pertaining to trivial systems is thus only its special case.

In the present work, we reveal the many faces of structure inversion symmetry breaking in TCI/NI heterostructures and demonstrate their intricate effect on band topology and topological surface and interface states both by theory and experiments. The system under investigation consists of $\text{Pb}_{1-x}\text{Sn}_x\text{Se}$ topological insulator quantum wells (QWs) confined on one side by a NI barrier layer and on the other by vacuum. $\text{Pb}_{1-x}\text{Sn}_x\text{Se}$ is a key member of the SnTe class of topological crystalline insulators (TCI)^[31–34] and features a non-trivial band topology when the Sn content exceeds a certain critical value below which it is a trivial insulator with a positive band gap (see **Figure 2a**).^[32,35–38] The material has long been used for infrared lasers and photo detectors^[39–41] and tunable Dirac states in TCI/NI multilayers have been recently demonstrated.^[42] This provides excellent conditions for thermoelectric devices based on TSS hybridization effects as recently proposed.^[43] The particular virtue of the system is that the band inversion can be controlled by the composition. For this reason heterostructures with tunable topology can be created that can be further controlled by strain,^[44] doping^[35,45] and applied electric fields.^[11,16] Moreover, bulk

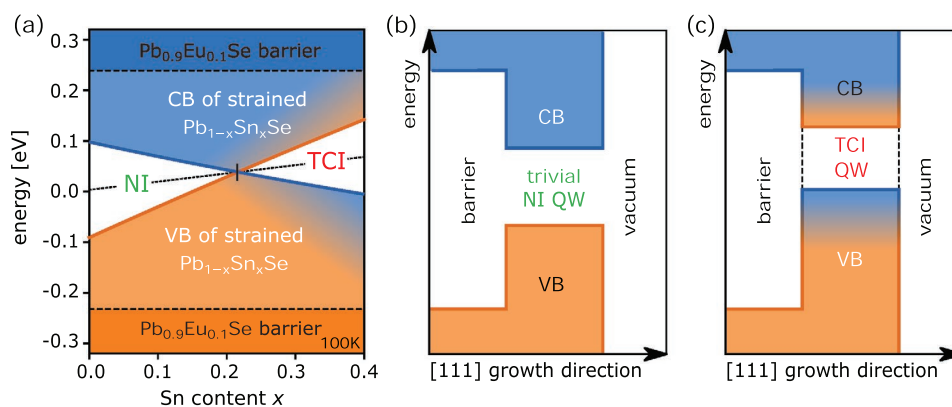


Figure 2. a) Band edges and band gap of pseudomorphic $\text{Pb}_{1-x}\text{Sn}_x\text{Se}$ on $\text{Pb}_{0.9}\text{Eu}_{0.1}\text{Se}$ (111) at $T = 100\text{ K}$ plotted as a function of Sn content x . The epitaxial strain due to the lattice mismatch is taken into account. The dotted line indicates the mid-gap position of $\text{Pb}_{1-x}\text{Sn}_x\text{Se}$ and the horizontal dashed lines the band edges of the $\text{Pb}_{0.9}\text{Eu}_{0.1}\text{Se}$ barrier. Blue (orange) coloring represents the cationic (anionic) character of the bands and the color change at $x = 0.22$ signifies the topological phase transition where the band gap is closed. At higher x the bands invert, that is, the gap changes sign, rendering $\text{Pb}_{1-x}\text{Sn}_x\text{Se}$ a topological crystalline insulator (TCI). The panels on the right present the schematic band diagrams for the b) trivial and c) non-trivial TCI cases of the $\text{Pb}_{1-x}\text{Sn}_x\text{Se}/\text{Pb}_{0.9}\text{Eu}_{0.1}\text{Se}$ heterostructures grown along the [111] growth direction.

$\text{Pb}_{1-x}\text{Sn}_x\text{Se}$ is inversion symmetric due to the rock salt structure so that inversion symmetry breaking can only be induced by imbalances of the surface and interfaces.

Here, we focus on the effect of structure inversion asymmetry stemming from different roots and demonstrate how the energy spectrum of the TSS and quantum confined states depends on the topological phase of the material as well as layer thickness and surface condition. In particular, we reveal that the SIA leads to a conventional Rashba splitting in trivial and thin TCI QWs, while in thicker QWs it causes a splitting of hybridized topological states. We further demonstrate that the splitting can be tuned by the surface termination, which provides an effective means of controlling the spin polarization. Our results are important for spintronic devices based on TCI materials, because all relevant factors governing their performance such as magnitude of spin splitting, spatial localization of the spin polarized states and the value and position of the hybridization gap can be effectively controlled.

2. Sample Structure and Experiments

The heterostructures here investigated were grown by molecular beam epitaxy on BaF_2 (111) substrates (see Experimental

Section). They consist of thin $\text{Pb}_{1-x}\text{Sn}_x\text{Se}$ quantum wells of varying thickness and composition, grown on top of $\text{NI Pb}_{1-y}\text{Eu}_y\text{Se}$ barriers residing on fully relaxed PbSe buffer layers. The QW thickness was varied over a wide range from $d = 5$ to 40 nm and the Sn content from $x = 0\%$ to 40%, thus spanning the whole parameter space from a normal to a topological insulator. Alloying of Eu into PbSe strongly increases the band gap,^[46,47] reaching 470 meV for $\text{Pb}_{0.9}\text{Eu}_{0.1}\text{Se}$ at 100 K as used in this work. This yields an effective quantum confinement of the electrons for all compositions (Figure 2b,c)), while a good lattice match of better than 0.8% is retained. As a result, perfect 2D layer-by-layer growth is achieved, signified by pronounced reflection high energy electron diffraction (RHEED) intensity oscillations and smooth surfaces observed by atomic force microscopy (see Figure 3a,b).

The samples were characterized by high resolution X-ray diffraction, evidencing the high quality of the samples by the prominent finite thickness oscillations (satellite peaks) of the diffraction patterns as shown by Figure 3c–e). From these the QW thicknesses and compositions were derived. Moreover, the X-ray reciprocal space maps recorded around symmetric and asymmetric Bragg reflections (Figure 3c,d) reveal the perfect pseudomorphic heterostructure growth by the perfect alignment of the diffraction peaks along the [111]

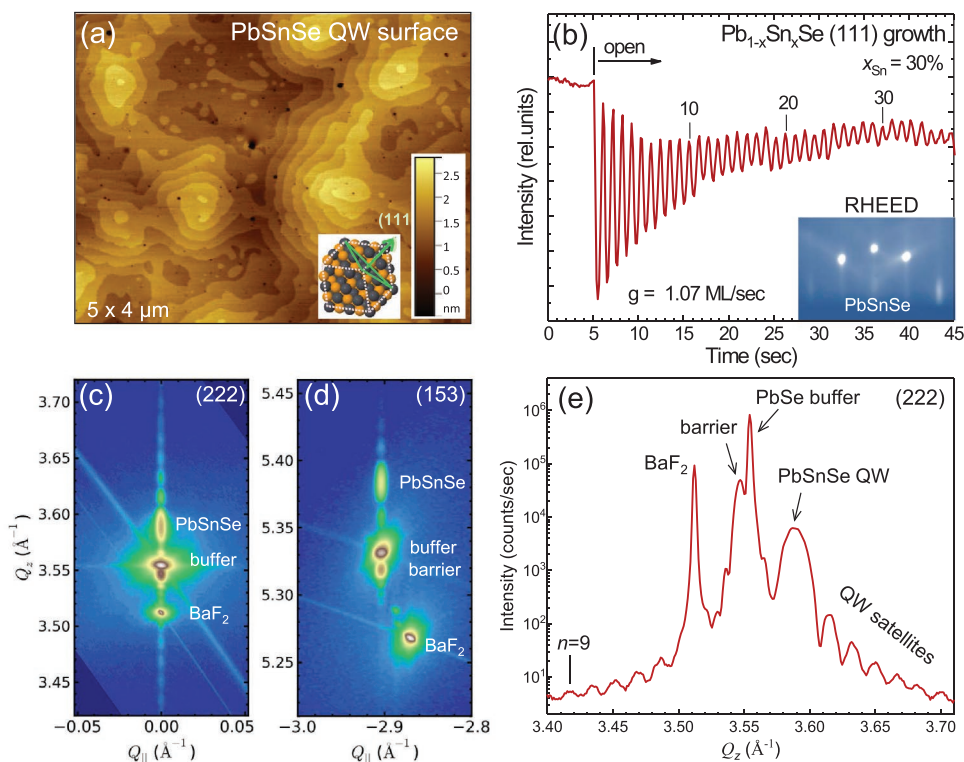


Figure 3. Growth and structural characterization of the topological insulator $\text{Pb}_{1-x}\text{Sn}_x\text{Se}/\text{Pb}_{0.9}\text{Eu}_{0.1}\text{Se}$ quantum well heterostructures. a) Atomic force microscopy image of a 20 nm QW with $x = 25\%$ on PbEuSe exhibiting exclusively surface steps of one monolayer height equal to 3.52 Å. The rock salt lattice structure of $\text{Pb}_{1-x}\text{Sn}_x\text{Se}$ in which the (111) atomic lattice planes alternate between cations (Pb,Sn) and anions (Se) is shown as insert. b) RHEED intensity oscillations observed during 2D layer-by-layer growth, where each period corresponds to the completion of one monolayer. The insert shows the 2D diffraction pattern observed at the end of growth. c–e) X-ray diffraction spectra of a $\text{Pb}_{0.67}\text{Sn}_{0.33}\text{Se}/\text{Pb}_{0.9}\text{Eu}_{0.1}\text{Se}$ QW with 40 nm thickness grown on a thick PbSe buffer layer on BaF_2 (111) substrate. Panels (c) and (d) display the reciprocal space maps recorded around the (222) and (153) Bragg reflection, and (e) the corresponding line scan along $Q_z = [111]$ normal to the surface. Pronounced satellite peaks of the QWs caused by finite thickness oscillations are visible to high order. This demonstrates the high quality and uniformity of the samples.

growth direction. The QWs are, thus, fully strained to the underlying buffer layer, which yields a tensile in-plane strain that varies linearly with Sn content to $\varepsilon_{\parallel} = 0.8\%$ for $x = 40\%$. Albeit small, its effect on the band gap and band alignments is taken into account in our model calculations (see Experimental Section).

The quantized 2D electron subbands and TSS were characterized by angle resolved photoemission spectroscopy (ARPES) and modelled by nearest-neighbor 18-orbital sp^3d^5 tight binding (TB) calculations with spin-orbit interactions included. The validity of the TB method for IV–VI TCI heterostructures has been proven previously.^[32,48] Due to the valley degeneracy of the IV–VI compounds, quantum confined states are formed at the four L-points of the Brillouin zone (BZ). For (001) or (110) films, these are projected onto the 2D BZ in pairs, whereas for (111) they are projected individually, one to the $\bar{\Gamma}$ -point and the others to three non-equivalent \bar{M} -points. In the following, we focus on the vicinity of $\bar{\Gamma}$ because the spectra around \bar{M} differ only in minor details (see Supporting Information). We recall that this is in contrast to pure SnSe, where the energy gap at \bar{M} oscillates as a function of film thickness, inducing a transition to a non-trivial 2D topological QSHE phase.^[10,11] In the Supporting Information, we show that this feature also occurs for ternary $Pb_{1-x}Sn_xSe$ but only for $x > 50\%$. Since at these compositions, the equilibrium crystal structure becomes orthorhombic, we have restricted here the Sn content to $x \leq 40\%$. This retains the good lattice matching between the QWs and buffer layers and yields the highest quality of the samples, which is essential for resolving the QW subbands even for large QW thicknesses by ARPES.^[49]

3. Results

3.1. Asymmetry of Confining Barriers

To assess the effect of SIA on the electronic QW states, we start with the generic asymmetry of the heterostructures arising from the different boundary conditions and confining barriers, defined by the connection to vacuum at the top surface and to the $Pb_{1-x}Eu_ySe$ barrier on the bottom interface. This SIA obviously involves only the very close vicinity of the boundaries, for which reason the resulting symmetry breaking is expected to affect the most the electronic states with high amplitude at the surface/interface. The pronounced effect of the different boundary conditions is demonstrated by **Figure 4**, where we compare the spectral function at the QW surface for free-standing, that is, symmetric $Pb_{1-x}Sn_xSe$ slabs with identical termination on both sides, with those of asymmetric $Pb_{1-x}Sn_xSe/Pb_{1-y}Eu_ySe$ heterostructures with anion termination on the vacuum and a solid state interface on the bottom side. To evaluate the changes across the topological phase transition, the calculations were performed for varying $Pb_{1-x}Sn_xSe$ compositions ranging from $x = 0\%$ to 40% , while the QW thickness was fixed to 18 nm. As one can see, for all cases quantized 2D subbands are formed in the conduction as well as valence band. With increasing Sn content, however, the band gap decreases and above $x = 22\%$ inverts such that a topological surface state emerges, characterized by a high spectral density at the surface and a linear energy-momentum dispersion. Moreover, its Dirac point is located well within the bulk band gap $E_{g, bulk}$ of $Pb_{1-x}Sn_xSe$ that is indicated by the horizontal dashed lines in Figure 4.

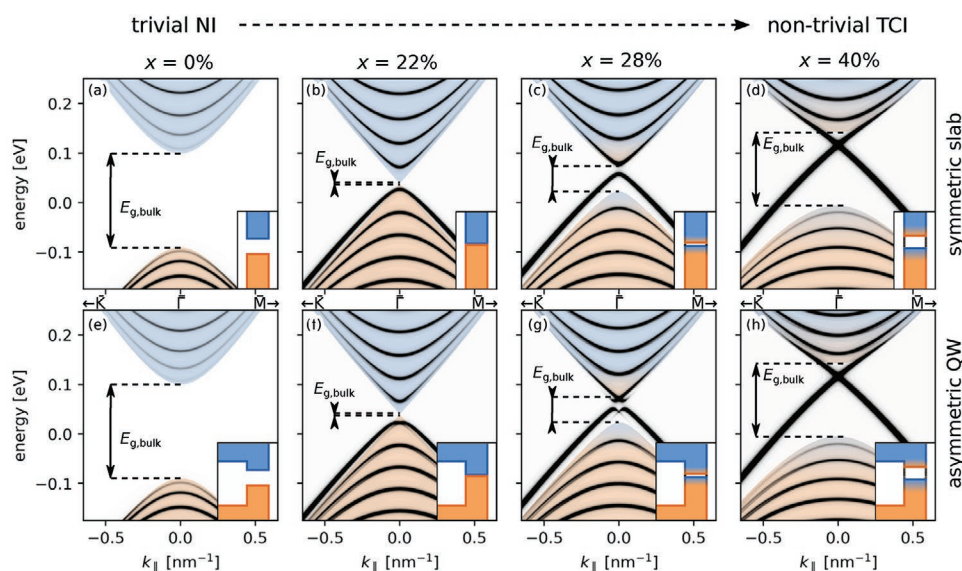


Figure 4. Spectral functions at the top surface of symmetric free-standing $Pb_{1-x}Sn_xSe$ slabs (top) and asymmetric $Pb_{1-x}Sn_xSe/Pb_{0.9}Eu_{0.1}Se$ quantum wells (bottom) for different Sn contents x , increasing from 0 to 40% derived by TB calculations. a, e) $x = 0$ corresponds to trivial QWs with positive band gap, b, f) $x = 22\%$ to near zero gap QWs, and c, d, g, h) $x = 28\%$ and 40% to topological nontrivial TCI QWs with inverted negative band gap (see Figure 2). The black lines represent the quantized electron states and topological boundary states. The orange/blue shading indicates the conduction and valence bands of the bulk material, where blue corresponds to a cationic; orange to an anionic band character. The calculations were performed for 18 nm thick QWs and $T = 100$ K and the inset in each panel depicts the schematic band diagram of the heterostructure system.

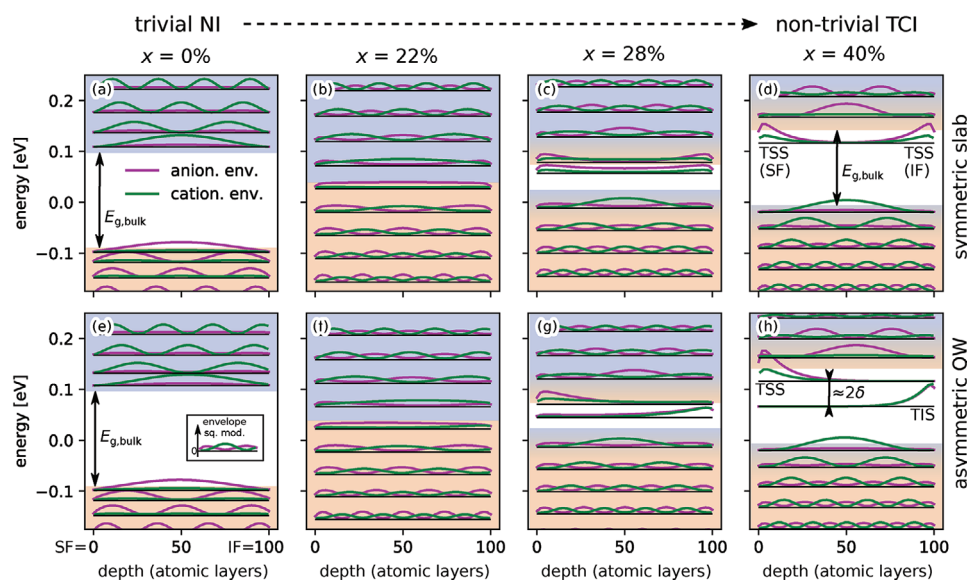


Figure 5. Squared moduli of the cationic (green) and anionic (magenta) components of the wave function envelopes of the TB solutions at $k = 0$ for the structures shown in Figure 4, that is, for free-standing $\text{Pb}_{1-x}\text{Sn}_x\text{Se}$ slabs (top) and asymmetric $\text{Pb}_{1-x}\text{Sn}_x\text{Se}/\text{Pb}_{0.9}\text{Eu}_{0.1}\text{Se}$ QWs (bottom). Each member of the Kramers pair at $\bar{\Gamma}$ is represented by the same pair of probability envelopes and the horizontal lines denote the energy of each state. a,e) $x = 0\%$ corresponds to trivial QWs with positive band gap, b,f) $x = 22\%$ to near zero gap QWs, and c,d,g,h) $x = 28\%$ and 40% to nontrivial QWs with inverted negative band gap. The shading represents the bulk conduction and valence bands of the corresponding bulk material where blue and orange color corresponding to cationic, respectively, anionic character of the bands. The QW thickness was fixed to 18 nm for all cases, which corresponds to 100 atomic layers. The depth $d = 0$ corresponds to the top QW surface (SF) and the depth 100 to the bottom QW/barrier interface (IF).

For symmetric slabs without SIA (top row of Figure 4) the lowest quantum confined state smoothly transform into the TSS when the Sn content increases. For asymmetric QWs with unequal sides, however, the structure asymmetry induces a Rashba splitting of the lowest conduction and highest valence subbands along the k_{\parallel} direction as shown in the bottom row of Figure 4. Remarkably, this splitting is particularly pronounced just after the topological transition ($x = 28\%$, Figure 4g) where the bulk band gap is negative and small, whereas for QWs with larger bulk band gap, both positive (PbSe , $x = 0\%$) or negative ($\text{Pb}_{1-x}\text{Sn}_x\text{Se}$, $x = 40\%$), the splitting is essentially invisible and the spectra of the symmetric and asymmetric cases are almost indistinguishable.

To explain this observation we take a closer look at the wave functions of the quantized subbands and the topological surface/interface states (TSS/TIS). These are displayed in **Figure 5** in the form of probability densities associated with the wave functions, divided into the cationic (green) and anionic (magenta) components. We can see that for trivial QWs with positive and open band gap ($x = 0\%$ in Figure 4a,e), the wave functions all exhibit nodes at the film boundaries. This means that the impact of differences in boundary conditions is small, and for this reason, the wave functions are nearly identical for the symmetric and asymmetric cases. For the near zero gap QW case ($x = 22\%$, see b,f), however, the wave functions of the lowest (highest) energy state in the conduction (valence) band have a uniform amplitude throughout the QW and, in particular, a non-zero amplitude at both surfaces. This makes them more susceptible to asymmetries in the boundary conditions and nicely explains the strong enhancement of the Rashba effect observed in this case.

For the topological QWs with high $x = 40\%$ (Figure 5d,h), the TSS wave functions also exhibit pronounced maxima at the film boundaries. Thus, one would expect these states to be most sensitive by the boundary conditions. For asymmetric structures, however, the TSS wave functions split up in a Kramers pair of one (TSS) located at the top QW/vacuum surface and one (TIS) concentrated at the buried $\text{PbSnSe}/\text{PbEuSe}$ interface (see Figure 5h). Accordingly, the upper TSS mostly feels the boundary condition of the top surface, whereas the lower TIS that of the bottom interface. As a result, they do not couple much to each other and the main effect of SIA is to shift the TSS and TIS apart in energy by a value 2δ , as indicated in Figure 5h. We further note that the Dirac band of the TIS at the bottom interface is not visible in the spectral functions shown Figure 4h, because the amplitudes of these states' wave functions vanish at the surface. Much like in the case of NI QWs, the wave functions of higher 2D subbands in TCI QWs exhibit nodes at the boundaries (see Figure 5e,h). Accordingly, the higher subbands are not much affected by asymmetries in the interfaces and their Rashba splitting is negligible.

In the intermediate case of $x = 28\%$ the topological states extend more deeply into the bulk of the QWs than for $x = 40\%$ because their localization length is large. This allows for hybridization of the wave functions of the topological states from the opposite boundaries even for relatively large QW thicknesses as considered in Figures 4 and 5. As a result, the topological states are separated by the hybridization gap. For symmetric structures, they have equal and substantial weight on both the top surface and the bottom interface, as shown in Figure 5c. As such, these states are very susceptible to any SIA, which explains the significant Rashba splitting in Figure 4g. Much like

for $x = 40\%$, in asymmetric structures the topological surface/interface states become separated in space, see Figure 5g,h. For $x = 28\%$, however, their wave functions still have non-negligible weight on both QW boundaries and thus, both topological branches of the TSS and TIS can be discerned in the spectral function at the surface. In addition, the hybridization gap still persists, albeit shifted away from the $\bar{\Gamma}$ -point.

Considering the multi-valley band structure of $\text{Pb}_{1-x}\text{Sn}_x\text{Se}$ we have also looked at how SIA affects the spectral functions at the \bar{M} -points of the surface BZ to which the states of the oblique L-valleys are projected (at the $\bar{\Gamma}$ -point, only the longitudinal L-valley projects). The results are presented in the Supporting Information, demonstrating that the spectral functions at \bar{M} are very similar to those at $\bar{\Gamma}$. Due to the (111) QW orientation and the effective mass anisotropy, however, the perfect valley degeneracy of the bulk is lifted in the QWs. This leads to a larger energy level spacing at the \bar{M} -point. Moreover, due to the tensile QW strain, the states at \bar{M} are also shifted upward in energy and the bulk band gap is slightly increased. For these reasons, the $\bar{\Gamma}$ states are always lower in energy in the QW structures, in agreement with ARPES measurements shown in the Supplemental Information. The exact magnitude of all these effects depends on the Sn content because the effective mass anisotropy and strain varies with $\text{Pb}_{1-x}\text{Sn}_x\text{Se}$ composition.

3.2. Hybridization Effects

As shown above, the Rashba effect in the QWs sensitively depends on the coupling between the interfaces. This obviously depends not only on the bulk band gap, but also on the QW thickness, which controls the hybridization between the TSS located at the opposite QW boundaries. To quantify this effect, we take a look at QWs with different thicknesses and composition deep in the TCI regime ($x = 32\%$). The results are presented in Figure 6, where the spectral functions derived from TB calculations are compared with ARPES measurements, both obtained for asymmetric heterostructures.

As one can see in Figure 6a,e, for thin QWs the gap $E_{g, \text{hyb}}$ is widely open due to the strong hybridization between the TSS and TIS at the top and bottom surfaces. In addition, a large Rashba splitting appears due to the SIA resulting from the different barriers. Consequently, the hybridization gap is again located not at $\bar{\Gamma}$ but shifted to a finite k_{\parallel} wave vector. $E_{g, \text{hyb}}$ rapidly diminishes with increasing QW thickness (Figure 6b,c,f,g), and eventually a gapless Dirac cone with linear dispersion and full spin polarization appears, both in theory and experiments (see Figure 6d,h). Because the TB and ARPES maps represent the spectral density at the surface, for the thick QWs the Dirac cone corresponds to the TSS located at the top QW surface, whereas the Dirac cone of TIS at the bottom interface (green

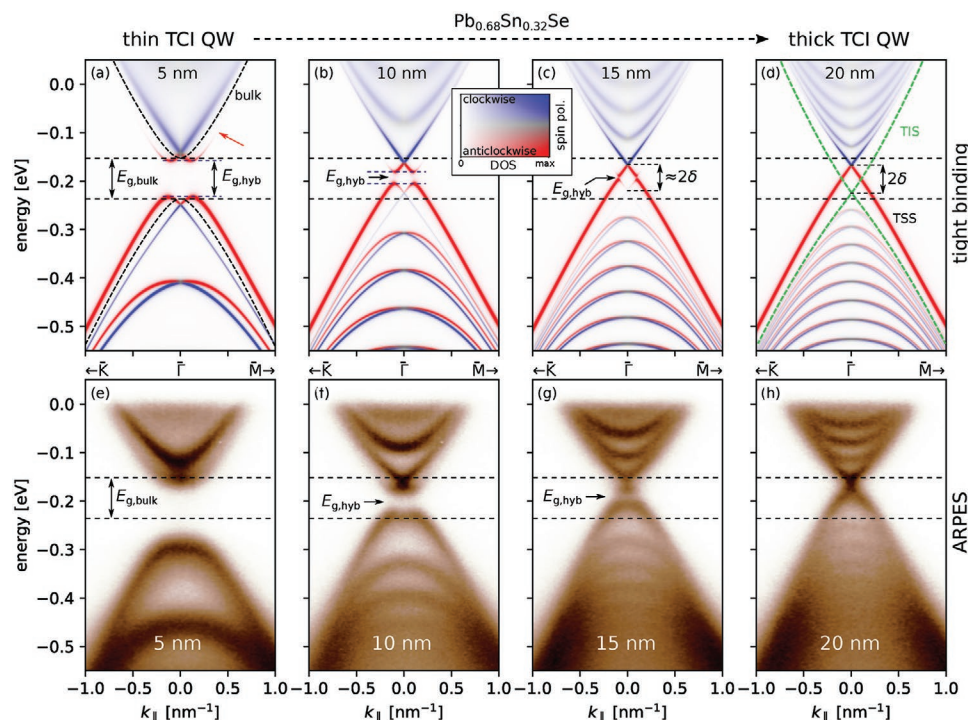


Figure 6. Spectral functions at the surface of asymmetric $\text{Pb}_{0.68}\text{Sn}_{0.32}\text{Se}$ quantum wells with thicknesses varying from $d_{\text{QW}} = 5$ to 20 nm obtained by TB calculations (top) and ARPES experiments (bottom). The quantum wells are terminated at the top by vacuum and on the bottom by a $\text{Pb}_{0.9}\text{Eu}_{0.1}\text{Se}$ barrier. The hybridization gap $E_{g, \text{hyb}}$ in the topological Dirac states, as well as the Rashba-type momentum splitting along k_{\parallel} due to the inversion asymmetry is seen both in theory and experiments. The asymmetry of interfaces also causes a splitting 2δ between the Dirac points of the top TSS and bottom TIS as indicated. For the 20 nm thick QW shown in d), the bottom TIS represented by the dashed green line is not visible due to negligible spectral weight at the surface. The degree of spin polarization in the TB maps is signified by the blue/red colors and it is calculated along the axis perpendicular to the corresponding \mathbf{k} vector. Blue corresponds to clockwise and red to anticlockwise spin polarization. The color intensity represents the weight of the spectral function at the top QW surface (see inset in (b,c)). The black dashed lines depict the bulk bands and bulk band gap of $\text{Pb}_{0.68}\text{Sn}_{0.32}\text{Se}$. Experiments and calculations were performed for $T = 100$ K.

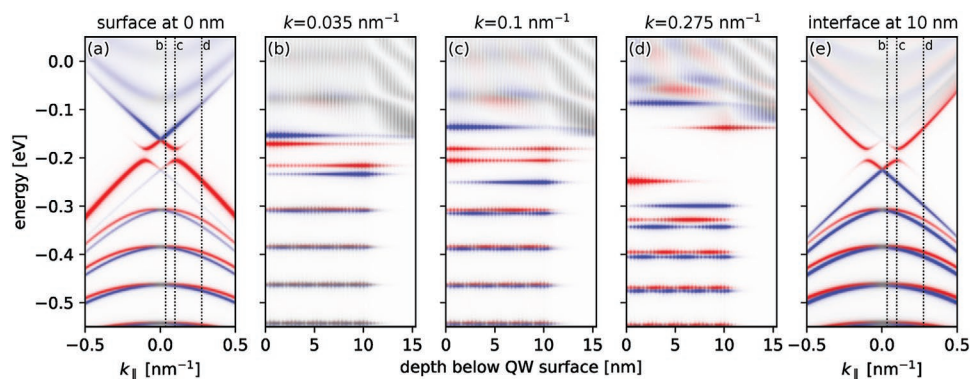


Figure 7. Spectral functions analogous to Figure 6 calculated a) at the top QW surface and e) the bottom interface, demonstrating the shift of the spectral weight from the surface to the interface and vice versa as a function of the wave vector k_{\parallel} . b–d) distribution of the spectral weight over the QW cross sections for different k_{\parallel} values that are indicated by the vertical dashed lines in (a) and (e). The structure is analogous to Figure 6b and consists of a 10 nm asymmetric $\text{Pb}_{0.68}\text{Sn}_{0.32}\text{Se}/\text{Pb}_{0.9}\text{Eu}_{0.1}\text{Se}$ QW. The color coding is the same as in Figure 6.

dashed line in Figure 6d) is invisible both in theory and experiments because its spectral weight at the surface is negligible.

For thin QWs, the surface dispersions exhibit lines vanishing at certain wave vectors k_{\parallel} away from $\bar{\Gamma}$ as indicated by the red arrow in Figure 6a. The origin of this effect arises from the change in surface spectral weight of the hybridized topological states as a function of k_{\parallel} as illustrated by Figure 7. Looking at the spectral functions calculated for the top (a) and bottom (e) surfaces, we find that for k_{\parallel} values where the spectral weight of the hybridized conduction band state diminishes at the top surface, it concomitantly gains weight at the bottom interfaces and vice versa. This means that the partition of the spectral weight between the top and bottom interfaces strongly changes with k_{\parallel} , as is illustrated by Figures 7b–d that display the spectral weight distribution across the QW cross section for different in-plane wave vectors indicated by the vertical dashed lines in (a) and (e).

For a thick QW, close to the bulk limit, the energy difference of the corresponding Dirac points at the two uncoupled QW boundaries approaches a fixed value 2δ . We recall that in absence of hybridization, the energetic position of the Dirac point $E_{\text{DP}}^{\text{surf}}$ at the (111) surface depends on the kind of surface termination,^[50] while the DP position $E_{\text{DP}}^{\text{int}}$ at the interface between the $\text{Pb}_{0.68}\text{Sn}_{0.32}\text{Se}$ QW and the $\text{Pb}_{0.9}\text{Eu}_{0.1}\text{Se}$ barrier is fixed by the atomic structure of the interface. In good approximation, the latter is determined only by the bulk band gaps $E_{\text{g, bulk}}$ and relative mid-gap positions V of the QW and barrier materials. Using an effective mass approximation^[51] to describe the sharp interface between the two media, the Dirac point energy at the TCI QW/barrier interface is obtained as

$$E_{\text{DP}}^{\text{int}} = \frac{E_{\text{g, bulk}}^{\text{B}} V^{\text{QW}} - E_{\text{g, bulk}}^{\text{QW}} V^{\text{B}}}{E_{\text{g, bulk}}^{\text{B}} - E_{\text{g, bulk}}^{\text{QW}}} \quad (1)$$

where the superscripts B and QW denote the barrier and the QW material, respectively, and $E_{\text{g, bulk}}^{\text{QW}}$ is negative in the band inverted TCI phase.

In thin QWs, the surface and the interface are close together and the topological states localized at the two boundaries interfere with each other. In the vicinity of the $\bar{\Gamma}$ -point, the resulting

electronic band structure can be modeled using the low energy Hamiltonian

$$H = \delta\sigma_3 + t\sigma_1 + v\sigma_3(k_x s_y - k_y s_x) + u(k_x s_y - k_y s_x) \quad (2)$$

where σ and s are the Pauli operators and the subscripts x, y indicate the directions parallel to the QW surface. Following Ref. [11] we omit the terms that are second and higher order in \mathbf{k} . The derivation of the model for the case of a TI slab can be found in Ref. [20].

Deep in the TCI QW regime, the interpretation of the terms in Equation (2) is simple. Namely, the basis states of Pauli operators σ_3 correspond to electrons localized on the two opposite QW boundaries, while the Pauli operators s act on Kramers pairs at $\bar{\Gamma}$ at each of the boundaries. Parameters $v \pm u$ define the Dirac velocities of the massless electrons at the two uncoupled boundaries of the layer which may differ due to a SIA. As previously stated, $\delta = (E_{\text{DP}}^{\text{surf}} - E_{\text{DP}}^{\text{int}})/2$. With decreasing QW thickness, the term proportional to t emerges, describing the hybridization between states on the surface and the interface.

Outside of the thick TCI QW limit, the parameters δ and u encompass the overall effect of SIA on the spectrum near the $\bar{\Gamma}$ -point, which includes the effect of the asymmetric potential on the basis states as well as mixing with the higher QW subbands. For ideal, inversion symmetric QWs, $\delta = 0$ and $u = 0$.

The eigenenergies in the conduction and valence bands are given by:

$$E_{\pm}^{\text{c}}(\mathbf{k}) = \pm u |\mathbf{k}| + \sqrt{t^2 + (v |\mathbf{k}| \pm \delta)^2} \quad (3)$$

$$E_{\pm}^{\text{v}}(\mathbf{k}) = \pm u |\mathbf{k}| - \sqrt{t^2 + (v |\mathbf{k}| \pm \delta)^2} \quad (4)$$

Accordingly, the energies of the hybridized Dirac points at the QW boundaries are at $E_{\text{DP}}^{\text{QW}} = \pm \sqrt{\delta^2 + t^2}$, and the hybridization gap emerges at a ring of quasi-momenta satisfying the condition $|\mathbf{k}| = k_R = |\delta/v|$, with a magnitude $E_{\text{g, hyb}} = 2t$. For perfectly symmetric structures with $\delta = 0$, the gap is exactly at $|\mathbf{k}| = 0$ in perfect agreement with Figure 4a–d. If, however, $\delta \neq 0$ the hybridization gap occurs at $|\mathbf{k}| = k_R > 0$, resulting in spectra displayed in Figure 6.

Note that while the term proportional to u has the form of a conventional Rashba Hamiltonian, here it describes only the difference in the Dirac velocities at the surface and at the QW/barrier interface, which is typically rather small. Thus, the main effect of SIA on the splitting of the hybridized Dirac cones comes from the term proportional to δ .

3.3. The Effect of the Polar Surface Termination

Due to the rock salt crystal structure, the native (111) surface of the $\text{Pb}_{1-x}\text{Sn}_x\text{Se}$ is fundamentally polar in nature because the (111) lattice planes are either occupied by group IV cations (Pb,Sn) or group VI anions (Se). In an idealized state, the (111) surface is thus, terminated either by cations or anions, which should have a profound influence on the SIA and the electronic surface states of the QWs. For the given sample preparation (see Experimental Section), the surface after decapping and annealing turns out to be anion (Se) terminated, similar as reported for SnTe .^[52–54] This leads to a p-type surface with the Dirac point above the Fermi level, depending on the annealing temperature. To vary the surface termination, we thus deposit

small submonolayer amounts of Sn onto the QW surface to tune the surface composition stepwise from anion to cation rich conditions.

The results are shown in **Figure 8**, where we present ARPES maps for near-zero-gap $\text{Pb}_{0.76}\text{Sn}_{0.24}\text{Se}$ QWs as a function of Sn coverage increasing from 0.1 to 0.5 monolayer (ML) from left to right, respectively. The experiments were performed for two different QW thicknesses of $d = 7$ and 18 nm, displayed in the top and bottom rows of the figure, respectively. At 0.1 ML Sn coverage (Figure 8a,g), we find that the Fermi level agrees with our previous reports on n-type bulk material.^[38,45] This indicates that a nearly “neutral” state of the surface is obtained. With increasing Sn coverage, that is, with increasingly cationic surface termination, the Fermi level shifts upward in energy and a strong Rashba splitting of the conduction and valence band states appears (see Figure 8c–f,i–l). This indicates a strong enhancement of the SIA induced by surface doping. While the Rashba splitting is negligibly small for the “neutral” surface it strongly increases up to a large value of $k_R = 0.26 \text{ nm}^{-1}$ at 0.5 ML Sn (Figure 8e). With the corresponding energy splitting of the Rashba bands obtained as $E_R = 30 \text{ meV}$ this yields a Rashba parameter as large as $\alpha_R = 2.2 \text{ eV\AA}$. This is almost

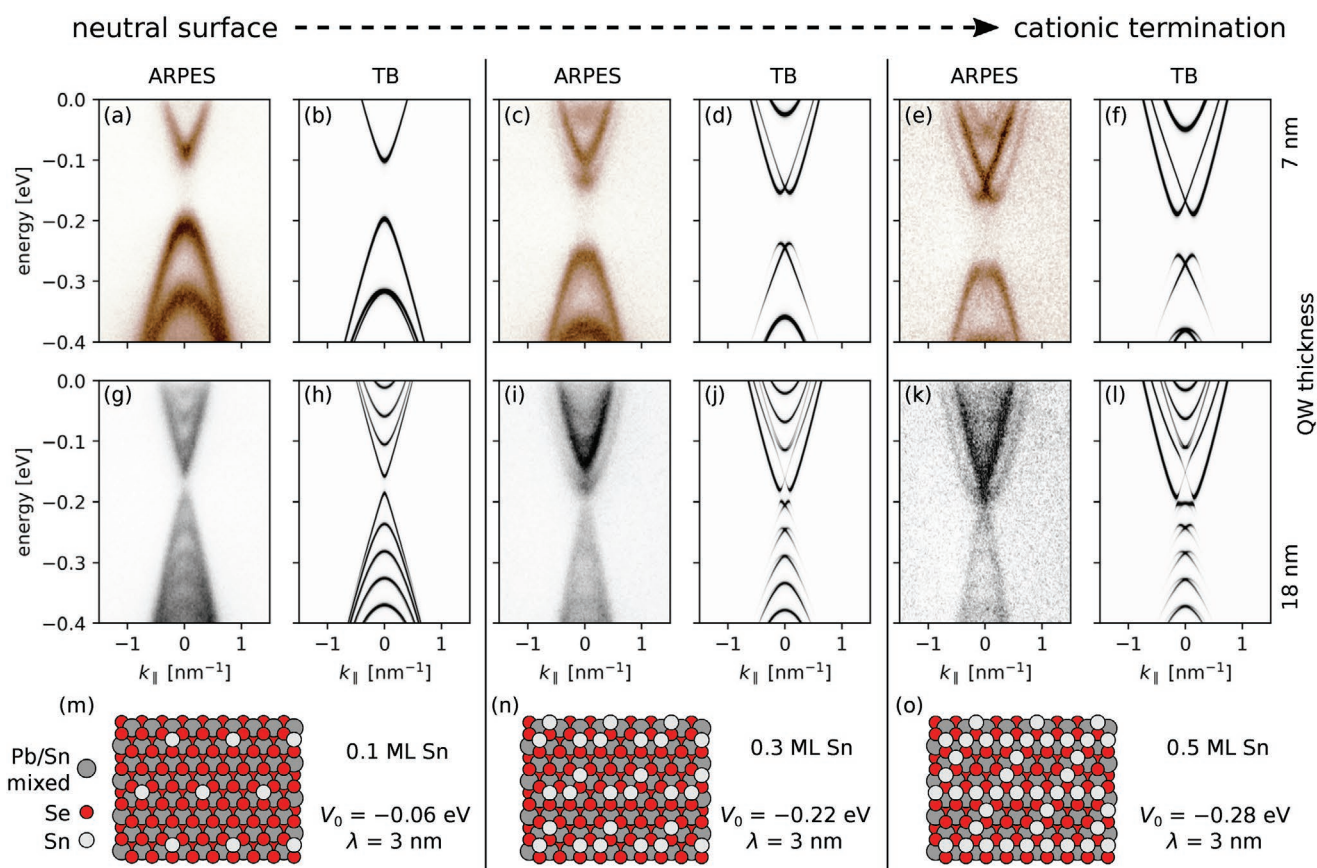


Figure 8. The effect of cationic surface termination for $\text{Pb}_{0.76}\text{Sn}_{0.24}\text{Se}/\text{Pb}_{0.9}\text{Eu}_{0.1}\text{Se}$ QWs with a–f) 7 nm and g–l) 18 nm well thickness observed by ARPES (a,c,e,g,i,k) and tight binding calculations (b,d,f,h,j,l) for $T = 100 \text{ K}$. In the experiments, the surface termination was changed by deposition of submonolayer amounts of Sn onto the QW surface, with the Sn coverage increasing from 0.1 to 0.5 ML from left to right, respectively. m–o) Atomic model structures of the surface employed for the TB calculations, where the extra Sn adatoms on top of the surface are represented by the white spheres. The fractions of Sn coverage and parameters V_0 and λ of the surface band bending potential caused by the Sn deposition are indicated. Theory and experiments were performed for $T = 100 \text{ K}$.

comparable to that of the giant Rashba effect reported for (111) bulk $\text{Pb}_{1-x}\text{Sn}_x\text{Te}$.^[45] The upward shift of the Fermi level with increasing Sn coverage shows that the Sn adatoms act as surface donors, leading to an increasing n-doping of the surface.

To model the influence of the varying surface termination, we created a refined TB model in which the additional fractional coverage of Sn adatom on the surface is taken into account as detailed in the Experimental Section. From the results, we find that the addition of Sn alone onto the surface does not yield the large Rashba splitting observed by experiments. For this, we have to take the additional attractive surface potential induced by the surface doping into account. This not only leads to an upward shift of the Fermi level at the surface as seen by ARPES, but also to a strong downward band bending at the surface. The electric field created by this potential gradient strongly enforces the Rashba effect.

To incorporate the band bending in our calculations, we impose an exponential Thomas–Fermi-like, screening potential $V(z) = V_0 e^{-z/\lambda}$ to the surface, following the procedure described in Ref. [45]. Here, V_0 denotes the height of the bending potential at the surface and λ the screening length. The results of the calculations are shown in panels (b,d,f, and h,j,l) of Figure 8, where the values of V_0 were adjusted to fit the calculation to the experiments while keeping $\lambda = 3$ nm constant. As indicated in (m–o) of Figure 8, V_0 substantially increases from nearly zero up to -0.28 eV for 0.5 ML Sn, and for the given V_0 values an excellent agreement between theory and experiments is obtained. This underlines the huge impact of the surface termination on the Rashba splitting of the TSS and reveals that by appropriate surface doping, the polarity of the clean anionic surface can be compensated and a nearly flat band potential condition with practically no Rashba effect can be obtained.

As a further proof of our model, additional control experiments were conducted in which we have used submonolayer Te-anion deposition to compensate the surface charge introduced

by the Sn-cations and thereby, revert the polarity of the surface. The result is shown in **Figure 9** for 0.3 ML Te deposited on top of the QW surface precovered with 0.4 ML of Sn. As one can see, after Te deposition the ARPES spectrum is nearly identical to that of the original “neutral” surface (Figure 8g). This unequivocally demonstrates the effective charge compensation between cation/anion adatoms residing on the surface. As a result, the large Rashba splitting induced by Sn can be completely erased by Te adatoms and, likewise, the original Fermi level restored. The effect of additional Te adatoms was incorporated in our calculations shown in Figure 9d, where the charge compensation between the Sn and Te adatoms was captured by changing V_0 to $+0.06$ eV compared to -0.27 eV for the 0.4 ML Sn covered surface (Figure 9b), by which again a good agreement between theory and experiments is obtained.

4. Discussion

To compare the different effects described above, we return to the Hamiltonian presented by Equation (2). We note that the form of the Hamiltonian is dictated by the symmetries of the QW, which in the case of $\text{Pb}_{1-x}\text{Sn}_x\text{Se}$ with rock-salt structure do not depend on the topological phase of the bulk material. In the TCI case, the topological boundary states of the QWs at $\bar{\Gamma}$ (see Figure 5d) correspond to eigenstates of σ_3 , and the parameter t is a measure of their hybridization. More generally speaking, the basis of σ operators corresponds to two energy levels at the $\bar{\Gamma}$ -point. In a trivial QW film, the eigenstates of σ_1 are the usual QW states of semiconductor heterostructures, one belonging to the highest valence and the other to the lowest conduction subband (Figure 5a). Accordingly, t in this case describes the QW band gap that is determined by the bulk band gap plus the quantum confinement energy due to the surrounding barriers. In all cases, v is the Dirac velocity, that is, the asymptotic slope of the energy-momentum dispersion well away from the

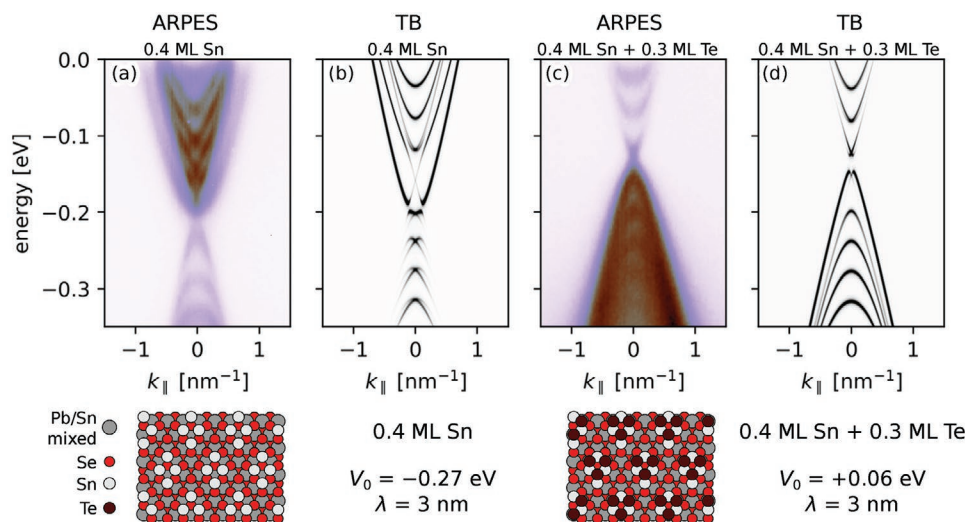


Figure 9. Effect of submonolayer Te deposition on the surface for a 20 nm $\text{Pb}_{0.76}\text{Sn}_{0.24}\text{Se}$ quantum well on $\text{Pb}_{0.9}\text{Eu}_{0.1}\text{Se}$ with 0.4 ML Sn predeposited on the surface. ARPES a) after 0.4 ML Sn and c) after 0.3 ML Te deposition are shown, and b,d) the corresponding tight binding calculations. In the lower part, the atomic configurations at the surface and the parameters of the surface band bending potential used for the TB calculations are depicted. Experiments and calculations are for $T = 100$ K.

$\bar{\Gamma}$ -point. v is imposed primarily by the bulk Dirac velocity of the QW material, as the bulk band structure of the rock-salt IV–VI compounds near the L-points is well approximated by a Dirac Hamiltonian.^[31,55] δ and u are corrections accounting for the inversion-symmetry breaking features of the system that comprise of the different contributions described above.

Moving from the trivial to the TCI case by increasing the Sn content above 25%, the lowest QW subbands in the conduction and valence bands smoothly transform into hybridized topological Dirac bands. In terms of the parameters of the Hamiltonian (2), this corresponds to a gradual decrease of t . Two effects contribute to the parameter δ : The asymmetric geometry and difference in the atomic structure of the sample surfaces, on the one hand, and the presence of an electrostatic band bending potential near the surface on the other. The magnitude of these contributions in $\text{Pb}_{1-x}\text{Sn}_x\text{Se}/\text{Pb}_{0.9}\text{Eu}_{0.1}\text{Se}$ QWs with cation surface termination is detailed in the Supporting Information, where it is described how the parameters t , δ , v , and u depend on the composition and QW thickness.

For the case of near-zero gap QW where t and δ can be of similar magnitude, as well as for trivial QWs where $t \gg \delta$, the energy spectrum obtained from the Hamiltonian (2) is reminiscent of the usual Rashba splitting in SIA systems with parabolic bands. To analyze this similarity, we calculate the Rashba parameter α_R for the conduction (valence) band as

$$\alpha_R^{c(v)} = \left| \frac{2E_R^{c(v)}}{k_R^{c(v)}} \right| \approx \left| \frac{\partial E^{c(v)}}{\partial k_x} \right|_{k=0} = \left| u \pm \frac{v\delta}{\sqrt{\delta^2 + t^2}} \right| \quad (5)$$

where in the last equality the $+(-)$ sign corresponds to the conduction (valence) band, and k_R and E_R to the momentum and energy splitting, respectively, as indicated by the inset of Figure 10a. Note that the approximate equality in the above formula is invalid for thick TCI QWs, for which $|\partial E^{c(v)}/\partial k_x|_{k=0} \approx |E_R^{c(v)}/k_R^{c(v)}|$.

Equation (5) is consistent with the fact that the Rashba splitting is greater for stronger SIA, the magnitude of which is represented in the model by parameters δ and u . With increasing Sn content in the QW the effective band gap and thus, t both decrease while δ and u typically increase for the types of SIA considered in this work (see Supporting Information).

In Figure 10 the values of k_R , E_R , and α_R corresponding to typical values of the parameters t , δ , and v , with $u = 0$ derived for the $\text{PbSnSe}/\text{PbEuSe}$ heterostructures are plotted as a function of the magnitude of the SIA, that is, of δ for different t values. Indeed, the Rashba constant α_R attains the lowest values for larger t , which corresponds to QWs made of a trivial insulator or very thin QWs made of near-zero-gap or TCI materials.

We remark that the description of the SIA effect in terms of conventional Rashba splitting is only valid when the two formulas for α_R presented in (5) give similar results, that is, when the dotted and the solid lines in Figure 10c, representing the two sides of the formula, match. To illustrate this further, in this regime ($t \gg \delta$ and $v \gg u$) we derive an effective model for conduction band up to second order in perturbation theory. It has the familiar form of the Rashba Hamiltonian

$$\tilde{H} = E_c + \frac{\hbar^2 \mathbf{k}^2}{2m^*} + \alpha_R (k_x s_y - k_y s_x) \quad (6)$$

with

$$E_c = t + \frac{\delta^2}{2t}; \quad \frac{\hbar^2}{2m^*} = \frac{v^2}{2t}; \quad \alpha_R = u + \frac{\delta v}{t} \quad (7)$$

where E_c is the energy of the Kramers pair at $\bar{\Gamma}$. In the trivial case, we can thus conclude that the spin splitting is primarily due to mixing of spin states within a single band.

The assumptions $t \gg \delta$ and $v \gg u$ can be valid also for sufficiently narrow TCI QWs and near-zero-gap QWs with sufficiently weak SIA. We find, however, that in these QWs for magnitudes of SIA considered in this work, typically $\delta \gtrsim t$ (see Supporting Information). In this case the two-band approximation (6) is invalid, and one should use at least four basis functions to analyze the SIA effect.

5. Conclusions

In conclusion, we have unraveled the effect of SIA on the electronic structure of epitaxial TCI quantum well heterostructures and their NI counterparts both by theory and experiments. SIA is intrinsic in thin film structures grown on a substrate as the film boundaries are different at the surface and film/substrate

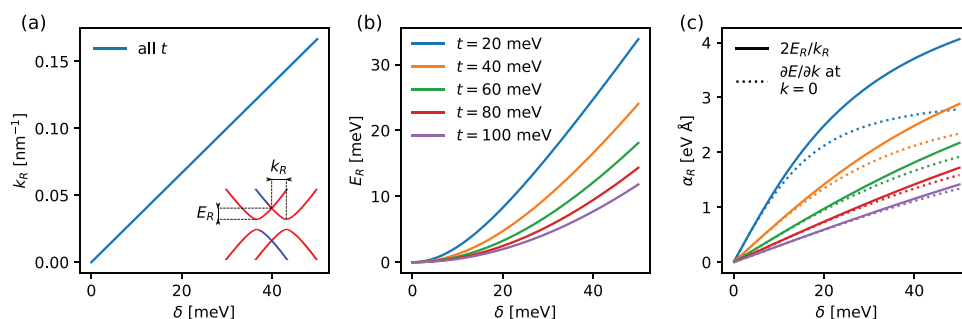


Figure 10. Rashba parameters of a) momentum splitting k_R , b) energy splitting E_R , and c) Rashba constant α_R plotted as a function of the parameters t and δ of the model Hamiltonian (2) for the range of typical values of the studied $\text{PbSnSe}/\text{PbEuSe}$ QW system, with $v = 3 \text{ eV Å}$ and $u = 0$. The colors in (c) correspond to the color legend in (b). In (c) also the slope $\partial E/\partial k$ of the energy dispersion at $\bar{\Gamma}$ (dotted lines) is compared with the standard definition of the Rashba constant (solid lines). The two sets of lines match for $t \gg \delta$.

interface. This induces a Rashba splitting in the QW electronic spectrum that strongly depends on the film thickness and the topological phase of the material, where the latter is controlled by the film composition. In TCI films the hybridization of topological boundary states opens up an energy gap in the electronic structure at the surface. The gap is moved away from the $\bar{\Gamma}$ -point of the surface BZ, which arises from the fact that the energetic position of the hybridized Dirac points as well as Dirac velocities are different at the surface and the buried interface. This is clearly observed by ARPES experiments and quantitatively explained by evaluation of the Hamiltonian for the vicinity of the $\bar{\Gamma}$ -point.

While in NI QWs the Rashba split bands are localized in the same region within the heterostructure, for thick TCI QWs the Rashba effect separates the spin-polarized bands not just in energy and momentum, but also *in space*. One band is localized at the top surface and the other at the buried interface. In thin TCI QWs, due to strong hybridization the effect of SIA is similar as in the NI case. For the lead tin chalcogenide TCI materials, the SIA is strongly enhanced by the highly polar nature of the (111) surface. The polarity depends on the surface termination that can be tuned by submonolayer cation/anion adatom (Sn/Te) deposition onto the surface. This results in a strong *n*, respectively, *p*-type surface doping, which induces a surface band bending described by a Thomas-Fermi screening potential that drastically enhances the Rashba effect and can be controlled by the adatom coverage.

Our analysis and experimental demonstrations are particularly important for spintronic devices based on TCI materials, because all relevant factors that govern their performance, like the magnitude of spin splitting, spatial localization of the spin polarized states and the value and position of the hybridization gap in momentum space depend strongly on the parameters here considered. In particular, we have not only revealed these effects for the first time in TCI heterostructures, but moreover demonstrated that the spin splitting sensitively depends on the material composition, quantum well width and structural asymmetry of the interfaces, as well as the surface termination. Thus, our findings open up a wide parameter space for tuning the properties of TCI systems. Last but not least, the particularly high sensitivity of the system to the structure asymmetry suggests that similar effects can be also achieved by externally applied electric fields as employed for device applications.

6. Experimental Section

Sample Growth: High quality epitaxial PbSnSe/PbEuSe heterostructures were grown in a Riber 1000 molecular beam epitaxy system at a substrate temperature of 300–350 °C under ultra-high vacuum conditions (10^{-10} mbar).^[41] Perfect 2D layer-by-layer growth was achieved as proven by pronounced RHEED intensity oscillations and smooth QW surfaces revealed by atomic force microscopy (see Figure 3). The heterostructures were grown on fully relaxed PbSe buffer layers predeposited on BaF₂ (111) substrates, followed by a 50 nm Pb_{0.9}Eu_{0.1}Se barrier layer onto which the Pb_{1-x}Sn_xSe QWs with different compositions ranging from *x* = 0 to 0.4 and thicknesses between 5 and 40 nm were deposited. The growth rates and compositions were controlled by adjusting the flux ratio of the PbSe, SnSe, Eu and Se effusion cells that were calibrated by micro balance measurements.^[41] The final structure was evaluated by X-ray diffraction using a Seifert diffractometer with CuK α_1 radiation and a channel cut Ge monochromator. Reciprocal space maps and radial diffraction scans as shown in Figure 3c–e were

recorded using a pixel detector array, from which the strain, thickness and composition of the layers were deduced.^[36,38,46]

Angle Resolved Photoemission Spectroscopy: The TSS and 2D subbands of the QWs were measured by ARPES performed at the UE112-PGM-2a-1² beam line of the BESSY II (Berlin, Germany). For excitation, horizontally polarized light with a photon energy of 18 eV was employed and photoelectron spectra recorded using a Scienta R8000 hemispherical analyzer with an energy resolution better than 5 meV. The measurements were carried out at pressures of around 10^{-10} mbar and temperatures of ≈ 100 K. To obtain high quality and clean surfaces, an amorphous Se capping layer was deposited on the surface *in situ* immediately after MBE growth to protect the surface against oxidation. This cap was subsequently desorbed at 320 °C at the synchrotron. In this way a clean Se terminated surface was obtained. For tuning of the surface termination submonolayer amounts of Sn and/or Te were deposited in steps of about 0.1 monolayers on top of the QW surface using Sn and Te evaporation sources.

Tight Binding Calculations: The tight binding approach was employed to model the electronic properties of the heterostructures within the virtual crystal approximation (VCA) using the parameters for PbSnSe derived by the procedure described in Ref. [48]. Since the TB parameters of EuSe and its alloys with PbSe were not available in literature, the parameters of PbSe were used with the energies of *p* orbitals adjusted to fit the measured band gap of the Pb_{0.9}Eu_{0.1}Se barrier material. The effect of the tensile strain in the QWs induced by the pseudomorphic growth was taken into account by scaling the hopping integrals to reproduce the experimentally measured band gaps. It was noted that the tensile strain affects the topological phase diagram of Pb_{1-x}Sn_xSe^[32,37] such that the band inversion and topological phase transition was slightly shifted to higher *x* values and thus, occurs in this case at *x* \approx 0.22 at *T* = 100 K as shown in Figure 2a. Schematic band diagrams of the trivial, respectively, non-trivial QWs on the PbEuSe barriers are depicted in Figure 2b,c. The temperature dependence of TB parameters was treated analogously as in Ref. [48], that is, they were scaled with the change of the lattice constant *a*₀. The spectral functions were calculated using the recursive Green's function method described in Ref. [56], where the samples were modeled as layers of Pb_{1-x}Sn_xSe on semi-infinite Pb_{0.9}Eu_{0.1}Se barriers. Unless otherwise specified, the spectral functions represent the total spectral weight on two full atomic layers at the surface, together with all deposited Sn and Te submonolayers.

Modelling of Surface Termination: To model the added submonolayer Sn coverage θ_{Sn} on the QW surface, ranging from 0 to 0.5 ML, an effective description was employed where the incomplete adlayer was replaced by a complete one and the hopping matrix elements between the adlayer and the QW were rescaled by $\sqrt{\theta_{\text{Sn}}}$ (see Supporting Information for details). The Sn sites were parameterized as cations of a SnSe bulk crystal in its rock salt phase. To verify this model, calculations were performed with Sn ions on top of the QWs, explicitly located at a fraction of sites in a periodic cell as depicted in Figure 8m–o. From this it was found that the spectral density was very weakly dependent on the details of the distribution of the adatoms, thus being well reproduced by the effective model. For the added Te surface adatoms on top of the Sn submonolayer, the parameters of Te anions in bulk SnTe were used, while the hopping matrix elements between the two incomplete adlayers were rescaled by $\sqrt{\theta_{\text{Te}} / \theta_{\text{Sn}}}$.

Supporting Information

Supporting Information is available from the Wiley Online Library or from the author.

Acknowledgements

This work was supported by the Polish National Science Centre, projects 2014/15/B/ST3/03833 and 2016/23/B/ST3/03725, as well as by the Austrian Science Funds (FWF), Project No. I 4493-N and P30960-N27. The work of V.V.V. in Poland was supported by the

Foundation for Polish Science through the IRA Programme co-financed by EU within SG OP. Calculations have been partially carried out using resources provided by Wrocław Centre for Networking and Supercomputing (<http://wcss.pl>), grant No. 330 and partially at the Academic Computer Centre in Gdańsk. J.S.-B. gratefully acknowledges financial support from the Impuls- und Vernetzungsfonds der Helmholtz Gemeinschaft under Grant No. HRSF-0067 (Helmholtz-Russia Joint Research Group).

Conflict of Interest

The authors declare no conflict of interest.

Data Availability Statement

The data that support the findings of this study are available from the corresponding author upon reasonable request.

Keywords

angle resolved photoemission spectroscopy, heterostructures, lead-tin chalcogenides, quantum wells, Rashba effect, structure inversion asymmetry, tight binding calculations, topological insulators

Received: October 27, 2020

Revised: February 15, 2021

Published online: March 29, 2021

- [1] M. Z. Hasan, C. L. Kane, *Rev. Mod. Phys.* **2010**, 82, 3045.
- [2] G. Wang, X.-G. Zhu, Y.-Y. Sun, Y.-Y. Li, T. Zhang, J. Wen, X. Chen, K. He, L.-L. Wang, X.-C. Ma, J.-F. Jia, S. B. Zhang, Q.-K. Xue, *Adv. Mater.* **2011**, 23, 2929.
- [3] X.-L. Qi, S.-C. Zhang, *Rev. Mod. Phys.* **2011**, 83, 1057.
- [4] Y. Ando, L. Fu, *Annu. Rev. Condens. Matter Phys.* **2015**, 6, 361.
- [5] C.-Z. Chang, J. Zhang, X. Feng, J. Shen, Z. Zhang, M. Guo, K. Li, Y. Ou, P. Wei, L.-L. Wang, Z.-Q. Ji, Y. Feng, S. Ji, X. Chen, J. Jia, X. Dai, Z. Fang, S.-C. Zhang, K. He, Y. Wang, L. Lu, X.-C. Ma, Q.-K. Xue, *Science* **2013**, 340, 167.
- [6] Y. Tokura, K. Yasuda, A. Tsukazaki, *Nat. Rev. Phys.* **2019**, 1, 126.
- [7] B. A. Bernevig, S.-C. Zhang, *Phys. Rev. Lett.* **2006**, 96, 106802.
- [8] B. A. Bernevig, T. L. Hughes, S.-C. Zhang, *Science* **2006**, 314, 1757.
- [9] M. König, H. Buhmann, L. W. Molenkamp, T. Hughes, C.-X. Liu, X.-L. Qi, S.-C. Zhang, *J. Phys. Soc. Japan* **2008**, 77, 031007.
- [10] S. Safaei, M. Galicka, P. Kacman, R. Buczko, *New J. Phys.* **2015**, 17, 063041.
- [11] J. Liu, L. Fu, *Phys. Rev. B* **2015**, 91, 081407.
- [12] E. J. Fox, I. T. Rosen, Y. Yang, G. R. Jones, R. E. Elmquist, X. Kou, L. Pan, K. L. Wang, D. Goldhaber-Gordon, *Phys. Rev. B* **2018**, 98, 075145.
- [13] M. Götz, K. M. Fijalkowski, E. Pesel, M. Hartl, S. Schreyeck, M. Winnerlein, S. Grauer, H. Scherer, K. Brunner, C. Gould, F. J. Ahlers, L. W. Molenkamp, *Appl. Phys. Lett.* **2018**, 112, 072102.
- [14] K. Yasuda, M. Mogi, R. Yoshimi, A. Tsukazaki, K. S. Takahashi, M. Kawasaki, F. Kagawa, Y. Tokura, *Science* **2017**, 358, 1311.
- [15] N. H. D. Khang, Y. Ueda, P. N. Hai, *Nat. Mater.* **2018**, 17, 808.
- [16] J. Liu, T. H. Hsieh, P. Wei, W. Duan, J. Moodera, L. Fu, *Nat. Mater.* **2014**, 13, 178.
- [17] J. Linder, T. Yokoyama, A. Sudbø, *Phys. Rev. B* **2009**, 80, 205401.
- [18] H.-Z. Lu, W.-Y. Shan, W. Yao, Q. Niu, S.-Q. Shen, *Phys. Rev. B* **2010**, 81, 115407.
- [19] C.-X. Liu, H. Zhang, B. Yan, X.-L. Qi, T. Frauenheim, X. Dai, Z. Fang, S.-C. Zhang, *Phys. Rev. B* **2010**, 81, 041307.
- [20] W.-Y. Shan, H.-Z. Lu, S.-Q. Shen, *New J. Phys.* **2010**, 12, 043048.
- [21] K. Ebihara, K. Yada, A. Yamakage, Y. Tanaka, *Phys. E: Low-dimensional Syst. Nanostructures* **2012**, 44, 885.
- [22] M. Okamoto, Y. Takane, K.-I. Imura, *Phys. Rev. B* **2014**, 89, 125425.
- [23] Y. Zhang, K. He, C.-Z. Chang, C.-L. Song, L.-L. Wang, X. Chen, J.-F. Jia, Z. Fang, X. Dai, W.-Y. Shan, S.-Q. Shen, Q. Niu, X.-L. Qi, S.-C. Zhang, X.-C. Ma, Q.-K. Xue, *Nat. Phys.* **2010**, 6, 584.
- [24] K. Nakayama, K. Eto, Y. Tanaka, T. Sato, S. Souma, T. Takahashi, K. Segawa, Y. Ando, *Phys. Rev. Lett.* **2012**, 109, 236804.
- [25] M. H. Berntsen, O. Götzberg, B. M. Wojek, O. Tjernberg, *Phys. Rev. B* **2013**, 88, 195132.
- [26] V. Litvinov, *Magnetism in Topological Insulators*, Springer, Cham **2020**.
- [27] Y. A. Bychkov, E. I. Rashba, *J. Exp. Theor. Phys. Lett.* **1984**, 39, 78.
- [28] R. Winkler, *Spin–Orbit Coupling Effects in Two-Dimensional Electron and Hole Systems*, Vol. 191, of *Springer Tracts in Modern Physics*, Springer, Berlin, Heidelberg **2003**.
- [29] S. D. Ganichev, L. E. Golub, *Phys. Status Solidi (b)* **2014**, 251, 1801.
- [30] G. Bihlmayer, O. Rader, R. Winkler, *New J. Phys.* **2015**, 17, 050202.
- [31] T. H. Hsieh, H. Lin, J. Liu, W. Duan, A. Bansil, L. Fu, *Nat. Commun.* **2012**, 3, 982.
- [32] P. Dziawa, B. J. Kowalski, K. Dybko, R. Buczko, A. Szczerbakow, M. Szot, E. Łusakowska, T. Balasubramanian, B. M. Wojek, M. H. Berntsen, O. Tjernberg, T. Story, *Nat. Mater.* **2012**, 11, 1023.
- [33] Y. Tanaka, Z. Ren, T. Sato, K. Nakayama, S. Souma, T. Takahashi, K. Segawa, Y. Ando, *Nat. Phys.* **2012**, 8, 800.
- [34] S.-Y. Xu, C. Liu, N. Alidoust, M. Neupane, D. Qian, I. Belopolski, J. Denlinger, Y. Wang, H. Lin, L. Wray, G. Landolt, B. Slomski, J. Dil, A. Marcinkova, E. Morosan, Q. Gibson, R. Sankar, F. Chou, R. Cava, A. Bansil, M. Hasan, *Nat. Commun.* **2012**, 3, 1192.
- [35] P. S. Mandal, G. Springholz, V. V. Volobuev, O. Caha, A. Varykhalov, E. Golias, G. Bauer, O. Rader, J. Sánchez-Barriga, *Nat. Commun.* **2017**, 8, 968.
- [36] G. Krizman, B. A. Assaf, M. Orlita, T. Phuphachong, G. Bauer, G. Springholz, G. Bastard, R. Ferreira, L. A. de Vaultier, Y. Guldner, *Phys. Rev. B* **2018**, 98, 161202.
- [37] A. J. Strauss, *Phys. Rev.* **1967**, 157, 608.
- [38] B. A. Assaf, T. Phuphachong, V. V. Volobuev, G. Bauer, G. Springholz, L.-A. de Vaultier, Y. Guldner, *npj Quantum Mater.* **2017**, 2, 26.
- [39] A. Katzir, R. Rosman, Y. Shani, K. H. Bachem, H. Böttner, H. Preier, in P. Cheo, (ed.), *Handbook of Solid-State Lasers*, Marcel Dekker, New York and Basel **1989**.
- [40] G. Bauer, M. Kriechbaum, Z. Shi, M. Tacke, *J. Nonlinear Opt. Phys. Mater.* **1995**, 04, 283.
- [41] G. Springholz, in M. Henini, (ed.), *Molecular Beam Epitaxy*, Elsevier, New York **2018**.
- [42] G. Krizman, B. A. Assaf, T. Phuphachong, G. Bauer, G. Springholz, G. Bastard, R. Ferreira, L.-A. de Vaultier, Y. Guldner, *Phys. Rev. B* **2018**, 98, 075303.
- [43] B. A. Bernevig, S.-C. Zhang, *Phys. Rev. Lett.* **2006**, 96, 106802.
- [44] X. Qian, L. Fu, J. Li, *Nano Res.* **2015**, 8, 967.
- [45] V. V. Volobuev, P. S. Mandal, M. Galicka, O. Caha, J. Sánchez-Barriga, D. Di Sante, A. Varykhalov, A. Khari, S. Picozzi, G. Bauer, P. Kacman, R. Buczko, O. Rader, G. Springholz, *Adv. Mater.* **2017**, 29, 1604185.
- [46] M. Simma, G. Bauer, G. Springholz, *Appl. Phys. Lett.* **2012**, 101, 172106.

- [47] T. Maurice, F. Mahoukou, G. Breton, S. Charar, P. Masri, M. Averous, R. Bisaro, *Phys. Status Solidi (B)* **1998**, 209, 523.
- [48] B. M. Wojek, R. Buczko, S. Safaei, P. Dziawa, B. J. Kowalski, M. H. Berntsen, T. Balasubramanian, M. Leandersson, A. Szczerbakow, P. Kacman, T. Story, O. Tjernberg, *Phys. Rev. B* **2013**, 87, 115106.
- [49] Z. Wang, J. Wang, Y. Zang, Q. Zhang, J.-A. Shi, T. Jiang, Y. Gong, C.-L. Song, S.-H. Ji, L.-L. Wang, L. Gu, K. He, W. Duan, X. Ma, X. Chen, Q.-K. Xue, *Adv. Mater.* **2015**, 27, 4150.
- [50] S. Safaei, P. Kacman, R. Buczko, *Phys. Rev. B* **2013**, 88, 045305.
- [51] V. Korenman, H. D. Drew, *Phys. Rev. B* **1987**, 35, 6446.
- [52] Z. Li, S. Shao, N. Li, K. McCall, J. Wang, S. X. Zhang, *Nano Lett.* **2013**, 13, 5443.
- [53] J. Wang, J. Liu, Y. Xu, J. Wu, B.-L. Gu, W. Duan, *Phys. Rev. B* **2014**, 89, 125308.
- [54] C. Yan, J. Liu, Y. Zang, J. Wang, Z. Wang, P. Wang, Z.-D. Zhang, L. Wang, X. Ma, S. Ji, K. He, L. Fu, W. Duan, Q.-K. Xue, X. Chen, *Phys. Rev. Lett.* **2014**, 112, 186801.
- [55] D. L. Mitchell, R. F. Wallis, *Phys. Rev.* **1966**, 151, 581.
- [56] M. P. Lopez Sancho, J. M. Lopez Sancho, J. Rubio, *J. Phys. F: Met. Phys.* **1985**, 15, 851.